Spectral Reflectance of Whitecaps: Instrumentation, Calibration, and Performance in Coastal Waters

KARL D. MOORE, KENNETH J. VOSS, AND HOWARD R. GORDON

Physics Department, University of Miami, Coral Gables, Florida

(Manuscript received 17 January 1997, in final form 9 June 1997)

ABSTRACT

A measurement system for determining the spectral reflectance of whitecaps in the open ocean is described. The upwelling radiance is obtained from a ship by observing a small region of the water surface over time using a six-channel radiometer (410, 440, 510, 550, 670, and 860 nm) extended from the bow of the ship. Downwelling irradiance is simultaneously measured and used to provide surface reflectance. The system includes a TV camera mounted beside the radiometer that provides a visual reference of surface events. Air/water temperature and wind speed/direction are also measured along with global positioning system data. Calibration procedures and radiometric characterization of the system for operation under different sky conditions and solar zenith angles are emphasized so that full advantage is taken of ship time whenever whitecap events occur. The radiometer was operated at sea and examples of the spectral reflectance of different foam types (thick foam layers to thin residual patches) generated by the ship's bow in coastal waters are presented and found to vary spectrally. The presence of submerged bubbles in the foam measurement results in a lower reflectance at the longer wavelengths. For wavebands in the visible region, the spectral reflectance values tend to equalize with higher reflecting foam from thicker foam layers.

1. Introduction

Remote sensing of the ocean by satellite requires accurate atmospheric correction. This is accomplished by measuring the upwelling radiance at a wavelength where the ocean is known to contribute very little or no radiance (Gordon and Wang 1994a). This is typically done at wavelengths beyond 700 nm (and sometimes at 670 nm) where the absorption properties of water are particularly strong. In the presence of whitecaps (whose coverage of the ocean surface varies primarily with wind speed), the ocean surface may no longer provide a negligible background for atmospheric correction at these longer wavelengths (Gordon and Wang 1994b). An understanding of the additional or augmented spectral upwelling radiance from whitecaps must be quantified not only at the wavelength used for atmospheric correction but at other wavelengths, particularly in the visible region, where spectral information provides a means of determining water content.

Previous authors have used a wavelength-independent foam reflectance of 50%–100% (Payne 1972; Gordon and Jacobs 1977; Maul and Gordon 1975) in conjunction with estimates of fractional coverage to determine the augmentation effect. Others have measured the spectral variation of foam in the laboratory using clear water and a variety of more turbid water types with various concentrations of detritus, sediment, etc. (Whitlock et al. 1982). Using still photography, Koepke (1984) established an efficiency factor that accounts for the diminishing reflectance and increase in area of the whitecap as it ages, thus providing a smaller augmentation effect than that of other studies.

Estimates of fractional coverage of whitecaps have been carried out previously by photographic methods, either from the air (Austin and Moran 1974; Ross and Cardone 1974) or from a stationary platform over the ocean surface (Monahan 1971; Toba and Chaen 1973; Koepke 1984; Bortkovskii and Novak 1993). The spectrum of foam reflectance has been determined in the laboratory (Whitlock et al. 1982), as well as for foam generated in the surf zone (Frouin et al. 1996). Whitlock's laboratory experiments showed a decrease in reflectance with increasing wavelength beyond approximately 0.8 μm. However, Frouin reported a much larger decrease in reflectance than Whitlock at the longer wavelengths: a 40% decrease at 0.87 μm, 50% at 1.02 μm, and 95% at 1.65 μm relative to the reflectance at 440 nm. The difference between the laboratory and field measurements is thought to be due to the stronger absorption properties of water at longer wavelengths acting on light reflected from submerged bubbles forced into the water by large waves (Frouin et al. 1996). It is important to note that *radiometric* measurements of the reflectance of actual oceanic whitecaps have not been

Corresponding author address: Dr. Kenneth J. Voss, Department of Physics, University of Miami, P.O. Box 248046, Coral Gables, FL 33124.
E-mail: kvoss@umiami.miami.edu

© 1998 American Meteorological Society

reported in the literature. Because of their important influence on atmospheric correction, and the suggested possibility that whitecaps may not be ''white'' (Frouin et al. 1996), we believe it is necessary to develop a system for acquiring reflectance data on real oceanic whitecaps.

The quantity of whitecaps covering the surface area of the ocean is detected as an augmentation in the upwelling radiance observed by the relatively low spatial resolution of a satellite pixel. To measure the spectral influence and magnitude of whitecaps in terms of a radiometric signal, the foam-free water-leaving radiance must be differentiated from the radiance contribution of whitecaps. This entails measurement of all visually observed foam types, that is, from thick highly reflecting foam generated immediately as the wave breaks to barely distinguishable thin residual and fragmented patches of foam as the whitecap decays back into ocean. (Note that here we use the term ''foam type'' to qualitatively describe the visual appearance of the white water. It is related to the magnitude of the reflectance of the foam; that is, a highly reflecting foam patch would be referred to as ''thick'' foam.) To measure the spectral reflectance of these foam types, particularly within the life cycle of an individual whitecap, requires an instrument of comparably high spatial and temporal resolution. Camera images of the ocean surface can provide a varied foam assortment, but determination of the foam-free background can be complicated by variation in sky reflectance toward the extreme regions of the image. This is particularly true when the imaging system is mounted on a platform and at an angle to cover as large an area of the water surface as possible. Use of a high-resolution imaging system for spectral measurements also requires a time delay between images of different wavebands, and the content of the spectral images may no longer be identical. A high-resolution imaging system from an airborne platform can provide greater coverage and a decrease in sky reflectance variation as the height above the water surface is increased, but at the cost of surface resolution. High-resolution spectral data of whitecaps is more feasible to acquire from a surface platform, particularly in the open ocean where flying an aircraft long distances and providing simultaneous ancillary measurements such as wind speed/direction and air/water temperature may become costly.

In this paper, a whitecap radiometer system for operation on board a ship or other surface platform is described. The spectral reflectance of the water surface is measured by a six-channel nonimaging radiometer with a narrow field of view and wavebands at 410, 440, 510, 550, 670, and 860 nm. The radiometer is deployed from the bow of a ship along with a TV camera to provide a visual reference of the radiometrically measured surface. In conjunction with the radiometer, a deck cell (cosine collector, see section 3a) monitors downwelling irradiance with matching wavebands, thus allowing estimation of the surface reflectance. By making many high spatial resolution measurements of the water surface at a fixed periodic rate, spectral data of individual whitecaps and their associated foam types (defined by their reflectance magnitude) can be obtained and an estimate of their frequency of occurrence determined. Measurement of the frequency of different foam types provides a value of the fractional coverage and the augmented spectral reflectance contribution of whitecaps to the water-leaving radiance as observed by ocean color satellites. In addition, the whitecap radiometer system acquires wind speed/direction and air/water temperature as well as global positioning system (GPS) information to provide universal time and location. Estimates of fractional coverage and augmented reflectance contribution can then be correlated to these parameters.

In section 2 we describe the whitecap instrument system and give particular attention to radiometric calibration for field use under various sky conditions and solar zenith angles in order to correct for slight deviations in the response of the deck cell's approximately cosine collector, and for the effects of spectral filter mismatch between channels in the deck cell and radiometer. Calibration for different sky conditions provides a robust system that takes full advantage of ship time and provides confident reflectance measurements of whitecaps whenever they occur. In addition, performance of the system is discussed and foam data generated by the ship's bow in coastal waters is examined.

2. Whitecap radiometer instrument description

Our strategy has been to measure whitecap reflectance from a surface platform such as a ship, either stationary or under way. The whitecap measurement system consists of a six channel radiometer aimed at the water surface; a downwelling irradiance collector with matching wavebands; water temperature and air temperature sensors; an anemometer to determine wind speed and direction; and a GPS to record location, GMT time, and determine ground speed and course heading. Taking many reflectance measurements of a small area of the ocean surface over time is equivalent to capturing a large field of view with high spatial resolution at one time.

The six-channel radiometer has wavebands at 410, 440, 510, 550, 670, and 860 nm and is aimed at the water surface with each channel covering approximately a 1° field of view. A TV camera (Sony SSC-C350 color CCD camera) with a greater field of view (~40°–50° using a 6-mm focal length video TV lens) is mounted beside the radiometer to provide a visual reference of radiometer measurements and is recorded on videotape using a videocassette recorder (Sony EV-C100). A triggerable analog switch has been implemented to allow individual TV frames to be date and time marked whenever the radiometer acquires data, thus providing a frame-by-frame reference.

The radiometer and TV camera assembly are extended over the bow of the ship as a unit by means of a boom. The boom comprises a number of segments of equal length and any number can be deployed to provide an extension from about 1 to about 10 m depending on the sea state

and at the same time ensure that optical shadowing and wind sheltering ship effects are minimized.

To provide reflectance measurements of the ocean surface, downwelling irradiance is measured by the deck cell at six matching wavebands, positioned on the ship to avoid shadowing. Wind speed and direction are measured by an anemometer placed in an unobstructed position toward the bow of the ship. Water temperature is measured with an accuracy of 0.1°C close to the surface by means of a small thermistor with signal conditioning circuitry to provide a linear and stable output. The thermistor's signal and power cable is fed down the center of a polypropylene rope with the thermistor exposed roughly 10–20 cm from the end of the rope. The buoyancy of the polypropylene rope keeps the thermistor at or near the surface, and the remaining few centimeters of the rope are flayed to ensure the thermistor does not skip out of the water as the ship moves. Air temperature is measured with an identical thermistor housed in a white plastic louvered cylinder to prevent direct solar heating. It is suspended from the bow of the ship close to the water surface but at a sufficient height to prevent contact with sea spray.

The analog signals from the radiometer, deck cell, anemometer, GPS, and water and air temperature sensors are sampled at a fixed periodic rate. Upwelling and downwelling radiometric data along with air/water temperature and wind speed/direction are sampled along with GPS data, GMT time, and location. The acquisition sequence is repeated until a time determined by the operator. Making many measurement of the reflectance from small areas of the ocean surface as the ship moves through the water allows one to estimate white water coverage as a function of wind speed and air/water temperature, as well as providing spectral information.

All cables from the various measuring components arrive at the electronics console, which is essentially an interface for individual cable connections as well as providing power and receiving analog signals. The analog signals are processed through differential amplifiers, to eliminate ground fluctuations that may originate over the long lengths of cable, before being digitized. The preconditioned analog signals are fed to a National Instruments NB-MIO-16XL acquisition board resident in a Macintosh Power PC. This acquisition board is configured to accommodate 16 referenced single-ended inputs and provide 16 bits A/D resolution. The acquisition board was set to run at the optimal sampling frequency of 55 kHz, resulting in a finite time delay (18 μs) between input channels. The effective integration time of the radiometer (and deck cell, etc.) was set to just under 30 ms by binning 100 samples per channel at this rate. This integration time is just less than a TV video frame period so visually recorded events could be correlated to radiometric measurements. Although the integration time is relatively short, the sampling frequency of the whitecap measurement system, being dependent on the GPS update frequency, was reduced to 0.5–1 Hz for the data acquired in this paper. The acquisition logic, processing sequence, and storage to file is controlled by LabVIEW software. The software also provides graphing and numeric display capabilities of the data as it is acquired. Data acquisition is allowed to free run and is halted at a time determined by the operator. Data files of various sizes are subsequently read into a statistical software package (Matlab) to produce detector background corrected and radiometrically calibrated reflectance values of the ocean surface along with air/water temperature and wind speed profiles.

a. The radiometer

Each channel of the radiometer consists of an optical tube aligned parallel to one another. Light entering each channel passes through a BK-7 window with a broadband AR coating. Behind this window, light for each channel is collected by a 25-mm-diameter, 100-mm focal length achromat with a broadband AR coating. The converging light passes through a 10-nm bandpass spectral interference filter. Behind the interference filters, broadband blocking filters are included to enhance out-of-band blocking of unwanted light. The field of view for all channels ($\sim$1°) is set by a 1.8-mm pinhole aperture placed at the focal point of the lens with the active area of the detector positioned 1.5 mm behind the focal plane. The detector for each channel is a silicon photodiode (Hamamatsu S1406-04) packaged with an integrated operational amplifier. The voltage output is fed into a low noise precision opamp (Analog Devices PM-1012GP) with a gain appropriate to each channel to offset variation in photodiode spectral response before being sent to the electronics console. Power ($\pm$12 V dc) sent to the radiometer is dc–dc converted and further regulated to supply $\pm$5 V dc to the photodetectors along with $\pm$12 V dc for the low noise precision opamps. Five of the six channels are arranged in a concentric fashion about the long axis of the housing with the 410-nm channel taking up the central position. The complete radiometer assembly is housed in a black anodized aluminum cylinder 30 cm in length and 11-cm diameter (see Fig. 1). These dimensions include an extension hood (5 cm in length) that is provided to prevent rain falling on the window and to reduce light that may be reflected and refracted by sea spray and salt deposits that inevitably collect on the window.

b. The deck cell

The deck cell is similar to the radiometer with the exception of the collection optics and its housing. The deck cell utilizes a cosine collector with an approximately 5-cm-diameter white diffusive acrylic plastic disk (Rohm & Hass, no. 2447) protruding about 1 cm beyond a dark rigid PVC base. Moving radially outward, the base is terraced, increasing in height with radius to a diameter of 124 mm at which point the height is flush with the top of the acrylic disk. The protruding acryclic disk in conjunction with the terraced base defines a 2π field of view and provides a near-cosine response (section 3d).

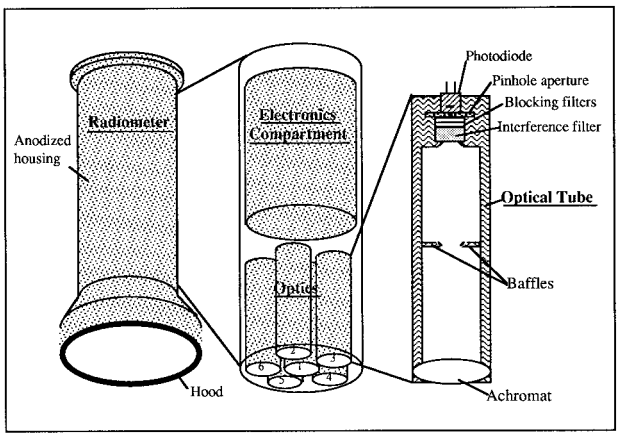

FIG. 1. A schematic of the whitecap radiometer and its components.

Five of the photodiodes with interference and blocking filters are arranged in a circle and slightly angled to view the center of the acrylic disk from behind, while the sixth photodiode–filter assemblage is centered behind the acrylic disk. In this way the cosine response is common to all channels of the deck cell. Unfortunately, because this arrangement exposes the interference filters to a relatively large field of view (16.6°–24°), both the spectral centers and widths of the instrument's response will differ from the nominal characteristics of the filters. This is discussed in detail in section 3e. The photodiodes, electronics, and optical filters are identical to the six channels in the radiometer but with a different gain on the precision opamps and with different optical apertures to accommodate the spectral variation of the downwelling light and detector response.

The 15-cm diameter by 13.5-cm-long cylindrical housing is made from rigid PVC plastic mounted in a two-axis gimbal. The bottom base plate of the housing is made from lead and in combination with the gimbal mount helps the cosine collector maintain a horizontal attitude despite any low-frequency small amplitude rocking motion of the test platform.

3. Radiometric calibration

a. Reflectance calibration

We define the reflectance R of the sea surface as

$$R = \frac{\pi L_{\mathrm{ws}}}{E_t},$$

where L_{ws} is the upwelling radiance from the water surface, and E_t is the downwelling irradiance falling on the sea surface. Here, E_t is defined to be

$$E_t = \int_0^{2\pi} \int_0^{\pi/2} L_t(\theta, \phi) \cos\theta \sin\theta \, d\theta \, d\phi,$$

where $L_t(\theta, \phi)$ is the total radiance (sun *plus* sky) falling on the sea surface from a direction specified by the polar and azimuth angles θ and ϕ, respectively. By design, a perfect irradiance instrument provides an electrical response to radiance $L_t(\theta, \phi)$ in a solid angle $\sin\theta \, d\theta \, d\phi$ that is proportional to $L_t(\theta, \phi)$. Such an instrument is called a "cosine collector." The deck cell approximates a cosine collector. The factor π is included by convention, so if $L_t(\theta, \phi)$ were independent of viewing direction (it is not), R would be the water surface albedo. In our experiments, L_{ws} is measured by the radiometer and E_t is measured with the deck cell. These are calibrated individually.

Laboratory radiometric reflectance calibration of the deck cell and radiometer was carried out using a calibrated 1000 W (FEL) quartz halogen lamp. The deck cell was positioned 50 cm from the lamp with the surface of its cosine collector perpendicular to normal incidence. For the radiometer, a Spectralon reflectance plaque was normally illuminated by the same lamp 50 cm away and viewed by the radiometer at a 45° angle. The reflectance of the plaque in this configuration is provided by the manufacturer and is approximately 0.95 from 400 to 870 nm when normally illuminated and viewed at a 45° angle. Background dark current readings were taken before and after each measurement. Absolute calibration was done in this manner before and after deployment in the field to verify radiometric stability.

b. Radiometric performance

To assess the quality of the calibration of the radiometer and deck cell, and to assess their efficacy in determining reflectance under the variety of natural sky conditions and solar zenith angles that occur in the field, the radiometer and deck cell were tested outside the laboratory. The radiometer was aimed vertically downward at a Spectralon reflectance plaque with the deck cell positioned beside the plaque. The plaque surface was level and at the same height as the flat surface of the deck cell cosine collector. The radiometer was positioned to avoid direct shadowing of the plaque and the deck cell, so that the radiometer blocked out only a small section of the sky. For the purpose of this test, it was assumed that the reflectance of the plaque during the laboratory calibration was unity in all of the channels (rather than the actual values of 0.957, 0.942, 0.944, 0.943, 0.944, and 0.949 for the channels from 410 to 860 nm, respectively). Thus, based on the laboratory calibration of the radiometer and the deck cell, one would expect the measurement in this test to yield a reflectance of unity in all channels.

Under overcast conditions with dark and bright patches of cloud passing overhead, variations in the measurement of the reflectance of the plaque were observed. A set of reflectance data was taken around noon with sky conditions going from one extreme (very overcast—sky totally covered and no distinct shadows observed) to another (direct sunlight breaking through a large clear patch with solar zenith angle ~30°). The variation (maximum to minimum) in reflectance values observed during these con-

ditions for each channel (410–860 nm) were 0.040, 0.045, 0.039, 0.050, 0.058, and 0.063 with the mean reflectance value for each found to be 0.987, 1.022, 0.969, 0.993, 1.001, and 1.122, respectively. Clearly, the calibration factors determined under laboratory conditions were not sufficient for measurements under real field conditions with a changing angular distribution of the light field. These simulated field measurements allow a rigorous understanding and calibration of the radiometric system, ensuring confidence in the reflectance data acquired under the variety of illumination conditions that are possible in field measurements. In the remainder of this section, we describe the steps taken to reconcile the measured plaque reflectance variation with illumination and describe the corrections required to apply the laboratory calibration to field measurements.

c. Linearity

The first step was to check the linearity of both the deck cell and radiometer to identify and eliminate any gross malfunctioning of the system. The photodiodes are reversed biased and as such should be highly linear. However, a damaged component, loose wire, or bad connection could exhibit nonlinearity at higher light levels that may not be seen at lower light levels of the laboratory calibration. As the gain and throughput of these instruments is specifically set for outdoor conditions, taking them into the lab where the proportion of blue light is comparatively low makes it difficult to cover the full dynamic range that might be encountered outdoors particularly for the shorter wavelength channels.

The linearity test was carried out by moving a constant light source specific distances from the instrument in question and the output signal recorded. In the case of the deck cell, the cosine collector was removed, and a diffusive surface of much greater transmissivity was put in its place to achieve an illumination intensity equivalent to that found outdoors on a clear day with the sun overhead. The diffusive surface was required to reduce nonuniform illumination effects observed by the off-axis channels when the lamp source (140 W) was brought close to the deck cell.

The radiometer, with a narrow field of view, was tested in much the same way but required a 1000-W lamp source and was tested intact without any alterations. A diffusive surface with low transmission was placed between the source and radiometer, at a fixed distance in front of the radiometer, to provide uniform illumination as the lamp source changed position. Both the deck cell and radiometer were found to be highly linear.

d. Angular response of deck cell and plaque

From the experiment performed under natural illumination, it was noted that the measured reflectance value of the plaque would sometimes increase and at other times decrease even though the downwelling irradiance remained constant. This suggested a possible sensitivity of the instrumentation to the angular distribution of the downwelling light field. A crude test performed with a clear sky and a large solar elevation also seemed to support this view. An opaque surface sufficiently large to continually block out the direct sun incident on both the deck cell and the reflectance plaque was raised and lowered to simulate a changing angular light field. By doing this, the reflectance value of the plaque was observed to change in a consistent manner with changing angular light field.

The angular response of the deck cell and the reflectance plaque was measured in the lab. With the lamp source (point) placed about 1.5 m from the surface of the cosine collector of the deck cell, the deck cell was rotated in 10° increments from normal incidence to $\pm 90°$. The resulting signal from the deck cell as a function of the rotation angle θ, normalized to $\theta = 0$, is the angular response $\mathrm{dc}(\theta)$.

To measure the appropriate response of the plaque, the plaque could be viewed at normal incidence with the radiometer and illuminated with a distant point source located at an angle θ with the normal. The variation of the radiometer with θ, normalized to $\theta = 0$, $\mathrm{RP}(\theta)$, is the reflectance response of the plaque. Alternatively, one may illuminate the plaque at normal incidence with a distant point source and view the plaque with the radiometer at an angle θ with respect to the normal. From the reciprocity principle (Chandrasekhar 1950) the response of the plaque is $\cos(\theta)$ times the radiometer output as a function of θ, for example, if the plaque were Lambertian the radiometer output would be independent of θ and $\mathrm{RP}(\theta) = \cos(\theta)$. We used the latter procedure here; however, the plaque could not be viewed from the normal due to the restrictive geometry of placing the radiometer in the same position as the source. Starting with the closest reasonably achievable viewing angle of 2° from the normal, subsequent measurements were taken at 5°–85° at 5° increments. For both the plaque and the deck cell, interpolation was performed with spline curves fit to the data.

Figure 2 compares the angular response from 0° to 85° for both the deck cell and reflectance plaque for all channels as a deviation from true cosine. (Note that the desired response of the deck cell should be true cosine to properly measure downwelling irradiance, and the response of the plaque, as defined above, would be true cosine if it were perfectly Lambertian.) In most channels, the response of the deck cell and reflectance plaque are similar with slight differences becoming apparent at larger angles of incidence. Although both deviate from true cosine, they appear to be close in response to each other with the exception of the poorer deck cell performance at 860 nm. For channels 410, 440, 510, and 550 nm, the deck cell appears to have an angular response that is closer to true cosine than the reflectance plaque, particularly at the larger angles. The 670-nm channel of the deck cell and reflectance plaque are the most similar yet both deviate from true cosine. In the 860-nm channel the deck cell response is much lower than the reflectance plaque response. Also,

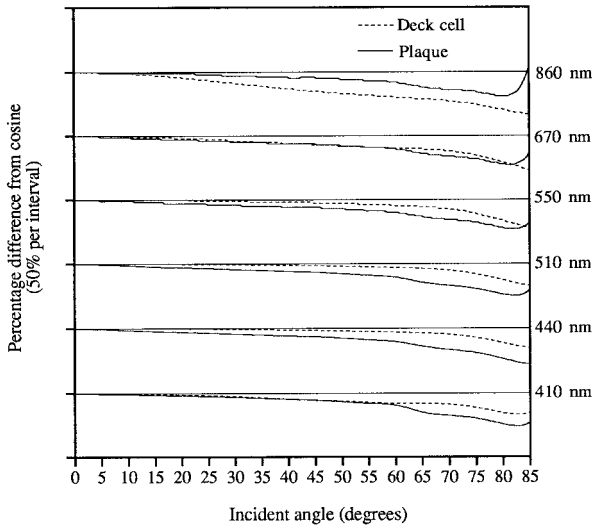

FIG. 2. Angular response of the deck cell and reflectance plaque in terms of deviation from true cosine response for 410-, 440-, 510-, 550-, 670-, and 860-nm channels. Each interval is 50%, and each waveband is offset by 50% for separation.

the reflectance plaque appears to have a consistent angular response in all channels.

To measure the correct reflectance of the calibrated reflectance plaque in the field, both the deck cell and reflectance plaque must be corrected for their noncosine responses to the particular downwelling angular light field distribution at the time of the measurements. To measure true (correct) reflectance R in each channel,

$$R = \frac{\pi L_t}{E_t},$$

we must determine L_t and E_t from the corresponding measurements made with the radiometer and the deck cell, L_{rad} and E_{dc}, respectively;

$$L_t = L_{\mathrm{rad}} r_{\mathrm{rad}},$$

where is L_{rad} is the radiance measured by the radiometer viewing the reflectance plaque and r_{rad} is the correction factor (due to deviation of plaque response from Lambertian) applied to L_{rad} to yield L_t, and

$$E_t = E_{\mathrm{dc}} r_{\mathrm{dc}},$$

where E_{dc} is the downwelling irradiance measured by the deck cell and r_{dc} is its correction factor. The correction factors are given by

$$r_{\mathrm{rad}} = \frac{\int \cos(\theta) L_t(\theta, \phi) \sin\theta \, d\theta \, d\phi}{\int \mathrm{RP}(\theta) L_t(\theta, \phi) \sin\theta \, d\theta \, d\phi} \Rightarrow \frac{\mathrm{TCR}}{\mathrm{RPR}}$$

and

$$r_{\mathrm{dc}} = \frac{\int \cos(\theta) L(\theta, \phi) \sin\theta \, d\theta \, d\phi}{\int \mathrm{DC}(\theta) L(\theta, \phi) \sin\theta \, d\theta \, d\phi} \Rightarrow \frac{\mathrm{TCR}}{\mathrm{DCR}},$$

where $\mathrm{RP}(\theta)$ is the reflectance plaque response, $\mathrm{DC}(\theta)$ is the deck cell response, and $L_t(\theta, \phi)$ is the downwelling radiance incident on the surface. TCR, RPR, and DCR are the true cosine, reflectance plaque, and deck cell responses, respectively, for a particular sky condition. Therefore,

$$R = \frac{\pi L_{\mathrm{rad}}}{E_{\mathrm{dc}}} C_r,$$

where $C_r = \mathrm{DCR/RPR}$, and the response correction factor C_r is dependent on sky condition $L_t(\theta, \phi)$. For example, to simulate the overcast sky condition the cardioidal expression $L_t(\theta, \phi) = 1 + 2\cos\theta$ is used. The resulting C_r in this case is provided in Table 1. Other sky conditions have also been simulated, for example, different solar zenith angles on a clear day. Clear day corrections were determined from measurements of the sky radiance distributions taken during clear sky conditions using a CIMEL suntracking photometer (Holben et al. 1997; J. Welton 1996, personal communication) to generate the radiance distribution for different solar zenith angles at 0°–

TABLE 1. Correction factors for each channel under different sky conditions due to the difference in solid angle response between deck cell and reflectance plaque.

	Channel 1 (410 nm)	Channel 2 (440 nm)	Channel 3 (510 nm)	Channel 4 (550 nm)	Channel 5 (670 nm)	Channel 6 (860 nm)
Overcast	1.0179	1.0566	1.0562	1.0420	1.0088	0.9195
Uniform	1.0243	1.0643	1.0629	1.0453	1.0088	0.9131
Sun 0	1.0063	1.0209	1.0210	1.0161	1.0038	0.9706
Sun 10	1.0034	1.0142	1.0141	1.0127	1.0085	0.9935
Sun 20	1.0069	1.0286	1.0272	1.0262	1.0135	0.9671
Sun 30	1.0061	1.0383	1.0398	1.0317	1.0093	0.9402
Sun 40	1.0014	1.0484	1.0484	1.0381	1.0035	0.9107
Sun 50	1.0046	1.0596	1.0621	1.0463	0.9996	0.8825
Sun 60	1.0163	1.0797	1.0829	1.0612	1.0061	0.8748
Sun 70	1.1061	1.1396	1.1407	1.0983	1.0493	0.8988
Sun 80	1.1140	1.1571	1.1443	1.0738	1.0207	0.8715

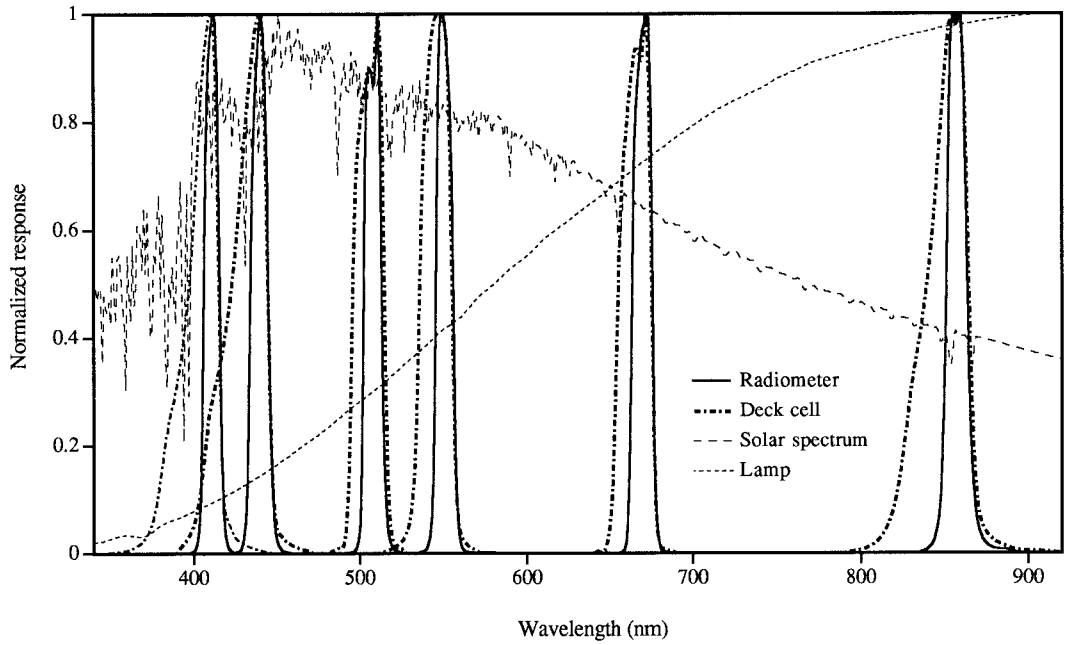

FIG. 3. Normalized radiometer and deck cell bandpass profiles with lamp and solar spectra.

80°. We found that the component of the downward radiance that mostly influences the correction factor is the solar beam itself. The resulting correction factors are also included in Table 1, which shows that applying the laboratory calibration relationship between the deck cell and the reflectance plaque to measure the plaque reflectance under field illumination is not valid.

e. Filter response

In addition to characterizing the effect of the angular response mismatch of deck cell and reflectance plaque under different sky conditions, the spectral filter response must also be examined. A monochromator using a 1000-W lamp source was used to determine the bandpass characteristics of each channel in both the deck cell and the radiometer. The monochromator output bandwidth was set to 1 nm to profile the nominal 10-nm bandpass of each filter assemblage. Measurement of the bandpass filters in each channel of the radiometer was a straightforward process. However, for the deck cell the amount of light passing through the diffusive acrylic material of the cosine collector was too small to afford any appreciable signal and was removed as before.

In order to normally illuminate the filter assemblages in the deck cell, the deck cell housing had to be angled with respect to the monochromatic output beam since the filter assemblages and their photodiodes (with the exception of the center photodiode–filter assembly) are purposely angled to view the center of the cosine collector. This action subsequently raised the question of the viewing angle of the interference filters inside the deck cell. The back of the cosine collector subtends a half angle of approximately 28° to the photodiode detectors, and the field of view for each channel was established by the different sized optical apertures placed in front of the filters. They were originally intended to increase light throughput at the shorter wavelengths and to reduce the throughput at the longer wavelengths. The half-angle field of view for each deck cell channel was 24°, 23.5°, 18.5°, 18.4°, 16.6°, and 16.6° for channels 1–6 (410, 440, 510, 550, 670, and 860 nm).

From these measurements it became obvious that the interference filters would possess different bandpass and transmission characteristics than those measured under normal illumination conditions. As the actual bandpass profile of the deck cell channel could not be measured directly, due to insufficient light output from the monochromator with 1-nm resolution, the bandpasses were calculated. This involved accounting for the center wavelength shift to shorter wavelengths and the associated transmission drop off and bandpass broadening (Handbook of Optics 1995). The center wavelength shift, transmission drop, and bandpass broadening were weighted with the effective increase in light intensity contribution due to the increase in field of view of the back side of the uniformly illuminated cosine collector at larger angles. The photodiode spectral response was also considered.

The laboratory calibration procedure for the radiometer and the deck cell would account for the difference in spectral response *only* if the spectral profile of the lamp source in the lab was the same as the solar spectrum. Obviously it is not, and differences in the spectral profile of the lamp and solar spectrum must be accounted for with the broader bandpass of the deck cell channels. In Fig. 3, the radiometer and deck cell bandpass profiles (calculated) for

TABLE 2. Correction factors for different filter bandwidths of the radiometer and deck cell in going from laboratory to outdoor illumination conditions.

Channel 1 (410 nm)	Channel 2 (440 nm)	Channel 3 (510 nm)	Channel 4 (550 nm)	Channel 5 (670 nm)	Channel 6 (860 nm)
1.0008	0.9278	0.9839	0.9648	0.9884	0.9640

each channel are shown along with the normalized lamp source and solar spectral profiles. The difference in the estimate of reflectance will be affected by going from a laboratory calibration under the lamp source to operation outside under the different spectral weighting of the solar spectrum. In Table 2, the bandpass multiplication correction factors that have been calculated to offset the error in making reflectance measurements in the field are provided. The bandpass correction factors $C_{\mathrm{BP}}(\Delta\lambda)$ have been arrived at by calculating the ratio of the integrated product of the radiometer bandpass and the solar spectrum to the integrated product of the radiometer bandpass and lamp spectrum and dividing by the ratio of the integrated product of the deck cell bandpass and the solar spectrum to the integrated product of the deck cell bandpass and lamp spectrum,

$$C_{\mathrm{BP}} = \frac{\int_{\lambda}^{\lambda+\Delta\lambda} B(\lambda)L_{\mathrm{solar}}(\lambda)\, d\lambda}{\int_{\lambda}^{\lambda+\Delta\lambda} B(\lambda)L_{\mathrm{lamp}}(\lambda)\, d\lambda} \times \left(\frac{\int_{\lambda}^{\lambda+\Delta\lambda} \mathrm{DCL}(\lambda)E_{\mathrm{solar}}(\lambda)\, d\lambda}{\int_{\lambda}^{\lambda+\Delta\lambda} \mathrm{DCL}(\lambda)E_{\mathrm{lamp}}(\lambda)\, d\lambda}\right)^{-1},$$

where B is the bandpass response for a particular channel of the radiometer, DC the bandpass response for the same channel in the deck cell, and L_{lamp}, L_{solar}, E_{lamp}, and E_{solar} are the illumination profiles over $\Delta\lambda$ for the lamp source and sun, respectively.

f. Application of the correction calibration

In Fig. 4 the overcast sky and 30° solar zenith angle (sun 30) correction factors are applied to the reflectance data measurements taken for the plaque outside (as conditions varied from being very overcast to direct sunlight breaking through with 30° solar zenith angle and then eventually to broken conditions). The filter bandwidth correction has also been included. Due to the higher gain of the radiometer that is specifically set to measure the lower upwelling water reflectance signal and foam contributions, the 860-nm channel observing the approximate 95% reflectance plaque saturates when the sun appears from behind the clouds. This saturation has not been included in characterizing the 860-nm reflectance variation with sky condition.

Variation in the measured reflectance persists as the real sky condition departs from the modeled sky definition. The most noticeable benefit of these correction factors is in the 860-nm channel. Regardless of the sky correction, application of the angular response and filter bandwidth correction results in a mean measured reflectance (over the time period shown) of 0.9944 for overcast or 1.017 for direct sun with 30° zenith angle rather than the uncorrected mean reflectance of 1.122. The best description of an overcast sky and direct sun within the time series is shown on the figure. The application of the appropriate sky correction to the data taken under a valid sky description depicts a closer approximation to a reflectance value of unity in all channels. The standard deviation from a reflectance of unity for all channels is 0.0025 for the overcast condition and 0.0028 for the direct sun condition. Other regions of the time series are the result of sky conditions that are more difficult to describe and therefore to correct. The standard deviation of the variation in reflectance over the extreme sky conditions that occurred during the complete time series in Fig. 4 was 0.0081, 0.0089, 0.0086, 0.0101, 0.0127, and 0.0313 for channels 410–860 nm, respectively.

In Table 3, the amount of correction that has been applied to the measured reflectance for each channel and for both sky conditions (sun 30 and overcast) is provided. The resulting accuracy or percentage deviation from a reflectance value of unity is given in the last two columns. For example, the 860-nm channel data are corrected by 12.77% in the overcast data to read a corrected reflectance of 0.995 (i.e., 0.005% accuracy). The direct sun data are saturated for this channel.

g. Correction of field data

To make reflectance measurements of the water surface, only the deck cell requires solid angle response correction for different sky conditions. We have

$$R = \frac{\pi L_{\mathrm{ws}}}{E_t},$$

where R is the reflectance we wish to determine, L_{ws} is the upwelling radiance from the water surface (including contributions from below the surface) received by the radiometer, and E_t is the true downwelling irradiance. As before,

$$E_t = E_{\mathrm{dc}} r_{\mathrm{dc}},$$

where E_{dc} is the downwelling irradiance measured by

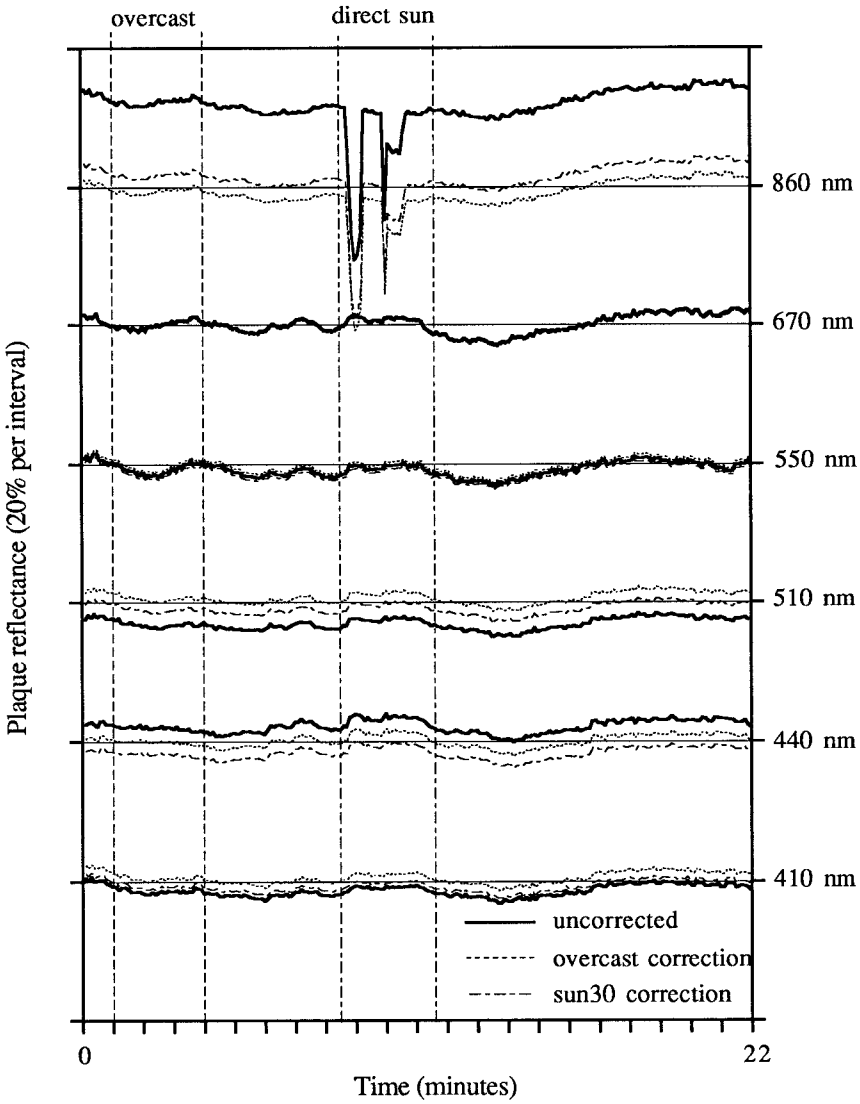

FIG. 4. Field test of system's ability to measure a plaque reflectance, as described in the text. Note that the 860-nm channel of the whitecap radiometer saturates when the plaque is illuminated by direct sun. Each interval represents a reflectance difference of 20%, and each waveband is offset by 20% to enable display.

the deck cell and r_{dc} is the sky correction factor that must be applied to the deck cell to have true cosine response, that is,

$$r_{dc} = \frac{E}{E_{dc}} = \frac{\int \mathrm{TC}(\theta) L_t(\theta, \phi) \sin(\theta)\, d\theta\, d\phi}{\int \mathrm{DC}(\theta) L_t(\theta, \phi) \sin(\theta)\, d\theta\, d\phi} = \frac{\mathrm{TCR}}{\mathrm{DCR}},$$

where

$$R = \frac{\pi L_{ws}}{E_{dc}} C_f \quad \text{and} \quad C_f = \frac{\mathrm{DCR}}{\mathrm{TCR}}.$$

Table 4 shows the field correction factors C_f the measured reflectance must be multiplied by in order to read correct reflectance. In addition, the C_{BP} correction for bandpass variations must be applied to the data.

4. Field test, results, and discussion

The initial measurements with the whitecap radiometer system were made to evaluate its performance and ability to provide a dependable database of air/water temperature, wind speed/direction, GPS information as well as radiometric and visual events recorded and date/time stamped onto video tape. The system was deployed on the RV *McGaw* for a 14-day cruise off the coast of Southern California. The ship visited a number of stations located in a small area on a daily basis to collect

TABLE 3. Effect of application of sky correction factor for each channel.

Channel	Overcast—amount of correction (%)	Direct sun—amount of correction (%)	Accuracy of overcast correction (%)	Accuracy of direct sun correction (%)
410	1.8	0.7	0.51	0.25
440	2.0	3.8	0.05	0.6
510	3.8	2.3	0.63	0.37
550	0.5	0.5	0.09	0.95
670	0.29	0.24	0.17	0.37
860	12.77	Saturated	0.005	Saturated

data for other oceanographic studies. Unfortunately, weather conditions were far from ideal for whitecap formation—primarily calm with mainly diffuse overcast days. However, data was taken of foam generated by the ship's bow as it moved from station to station. This provided a simple (and necessary) alternative for testing the system under field conditions. The radiometer was mounted at different positions over the side of the ship, providing a database for radiometric performance of the system and analysis of different stages of foam development.

Figure 5 is an example of the bow foam data obtained. In this example, the radiometer samples as the ship moves to its next station, and halfway through this time series the ship slows to a complete stop. When the ship has slowed to a speed where bow foam is no longer generated in the field of view of the radiometer, the water-leaving radiance and sky reflectance can be determined. The sky condition was completely overcast and slightly foggy, with a very calm water surface. This measurement of the foam-free water could then be subtracted from the foam reflectance to provide the spectral augmented foam reflectance contribution, although the real meaning of augmented reflectance in this case is lost due to the origin of the foam. Note that the mean reflectance of the bow-wave foam in the visible is approximately 0.6, which is in good agreement with the prediction of 0.55 made by Stabeno and Monahan (1986) for a lattice of thin-walled water bubbles.

In Fig. 6 the spectral reflectance of foam is shown in terms of different reflectance levels (intervals). These levels relate qualitatively to the visual appearance of different foam types, that is, progressing from thick fresh dense foam to residual thin patches, streaky foam, and submerged bubbles, the reflectance decreases progressively. For this differentiation, any reflectance spectrum with a particular value at 860 nm that falls within a reflectance interval is averaged. In the example shown, the set reflectance intervals are 0–0.04, 0.04–0.08, 0.08–0.12, 0.12–0.16, 0.16–0.20, 0.20–24, 0.24–0.28, 0.28–0.32, 0.32–0.36, 0.36–0.40, 0.40–0.44, 0.44–0.48, 0.48–0.52, 0.52–0.56, 0.56–0.60, and 0.60–1.00. The number of spectra averaged in any one interval is also provided. This gives an indication of the frequency of occurrence and the measurement accuracy in determining the spectral profile for the given reflectance level.

Foam data were also acquired under clear and sunny conditions where the effects of specular sun glitter were included. As the ship was there to service test station areas in a small grid, there were frequent changes in ship heading, making a fixed radiometric viewing angle with respect to the sun difficult to maintain. These changes in ship heading at random times of the day made the quantity of specular sun glitter more difficult to estimate. Some specular sun glitter was tolerable but depending on the illumination and viewing geometry it could at times radically affect the reflectance signal. In addition, it was difficult to avoid ship shadow, particularly at lower solar zenith angles. These experiences suggest that the best results with this system will be obtained under overcast conditions or where the ship maintains a fixed (and favorable) heading for a significant period of time, for example, a few hours. The effects of specular sun glitter in radiometrically discriminating white water from nonwhite water events is addressed elsewhere (Moore et al. 1997). However,

TABLE 4. Correction factors for each channel under different sky conditions due to deviation of solid angle response of the deck cell.

	Channel 1 (410 nm)	Channel 2 (440 nm)	Channel 3 (510 nm)	Channel 4 (550 nm)	Channel 5 (670 nm)	Channel 6 (860 nm)
Overcast	0.9529	0.9823	0.9809	0.9699	0.9373	0.8709
Uniform	0.9465	0.9773	0.9754	0.9624	0.9276	0.8563
Sun 0	0.9822	0.9939	0.9935	0.9894	0.9767	0.9512
Sun 10	0.9946	1.0007	1.0001	0.9988	0.9942	0.9866
Sun 20	0.9879	0.9999	0.9983	0.9959	0.9825	0.9557
Sun 30	0.9749	0.9940	0.9941	0.9874	0.9625	0.9125
Sun 40	0.9553	0.9893	0.9876	0.9791	0.9426	0.8699
Sun 50	0.9388	0.9814	0.9811	0.9694	0.9239	0.8339
Sun 60	0.9216	0.9705	0.9709	0.9539	0.9031	0.8042
Sun 70	0.9135	0.9545	0.9500	0.9246	0.8819	0.7749
Sun 80	0.8475	0.8906	0.8763	0.8382	0.7964	0.7072

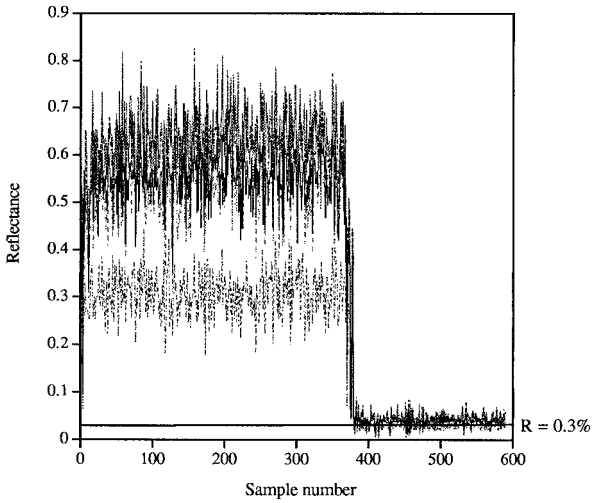

FIG. 5. Time series of foam data generated by bow of ship. The lower trace is for 860 nm. The rest (upper trace) are for the other channels.

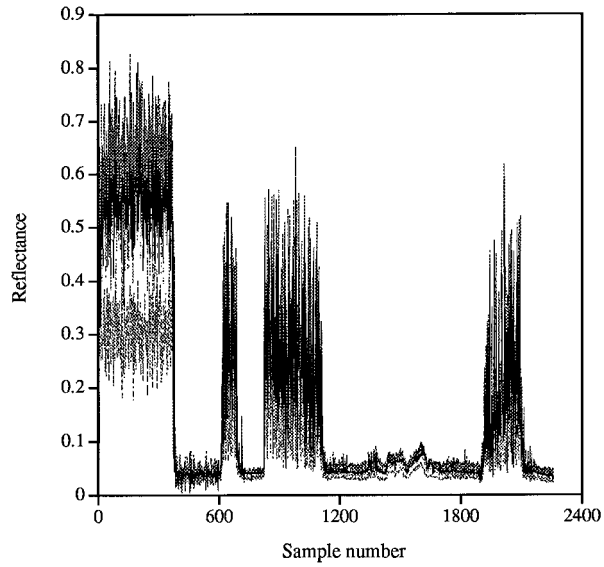

FIG. 7. Longer time series of foam data generated by ship showing periods when ship slowed and came to rest.

much of the data from this cruise was acquired under overcast sky conditions.

In Fig. 7 a collection of foam data taken at different times throughout a very overcast morning, starting at 0745, 1030, 1100, and 1200 LT (19 October 1995), was compiled into a single time series. The foam reflectance at the beginning of the time series is highest due to thicker foam generated by a higher ship speed. This first part of the time series is the same data used in Figs. 5 and 6, followed by starts and stops and lower ship speeds producing a varied set of foam reflectances. As before, reflectance levels relating to different foam types (or foam thicknesses) and the foam-free water-leaving radiance and sky reflectance (referred to as the foam-free water reflectance) are shown in Fig. 8 along with the number of spectral reflectance values used in the estimation of each interval.

The pronounced decrease in reflectance at the 670- and 860-nm channels compared to the blue–green is thought to be due to the strong absorbing properties of water at those wavelengths, particularly on light reflected from submerged bubbles (Frouin et al. 1996). Also of interest is the apparent reduction in the 410-nm channel. In Fig. 9 the spectral reflectance of intervals 2, 4, 7, 10, and 12 from Fig. 8 are shown. The spectral profiles

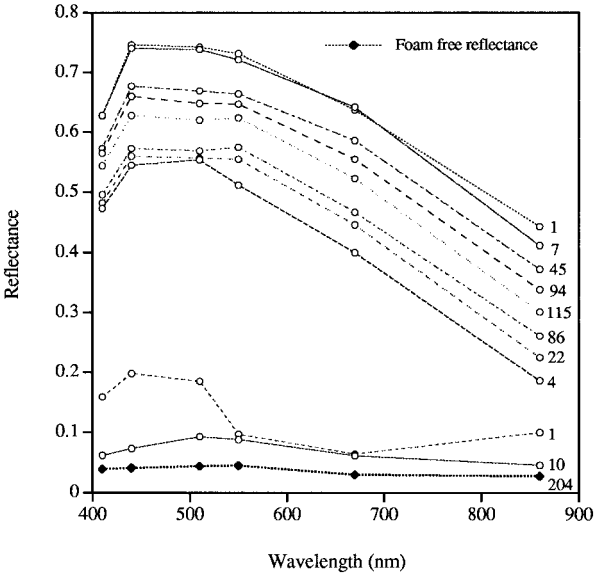

FIG. 6. Spectral reflectance of different foam types.

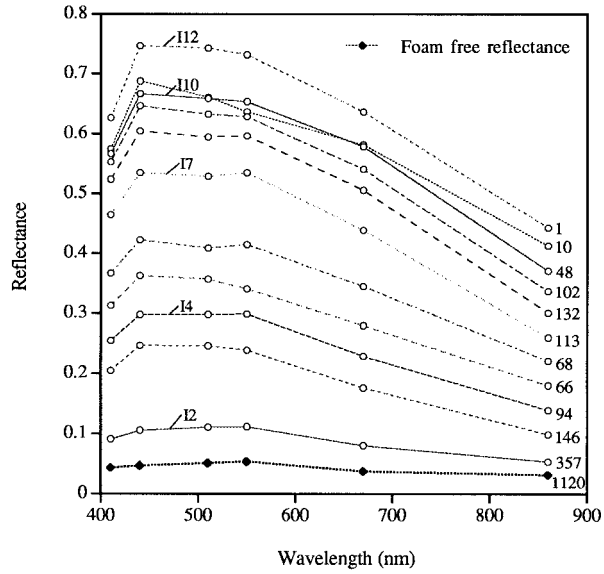

FIG. 8. Spectral reflectance of different foam types from larger time series. I2, I4, I7, I10 and I12 refer to reflectance intervals normalized at 440 nm in Fig. 10.

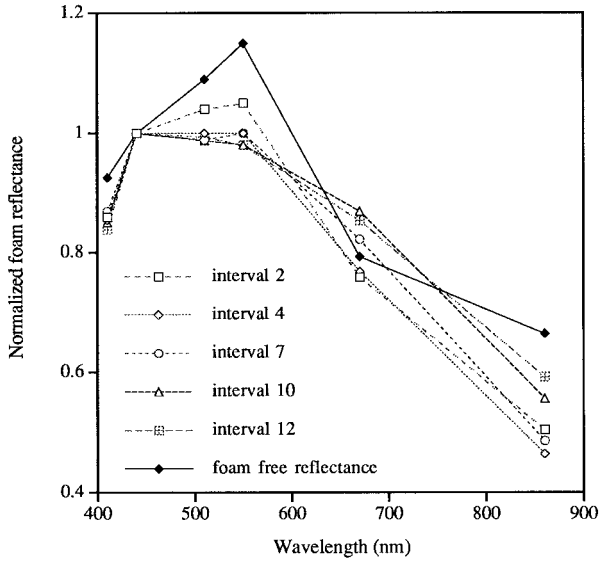

FIG. 9. Normalized spectral reflectance at 440 nm for different foam types taken from data used in Figs. 7 and 8. Note the spectral influence of the background water in measurement of the thinnest foam types in interval 2.

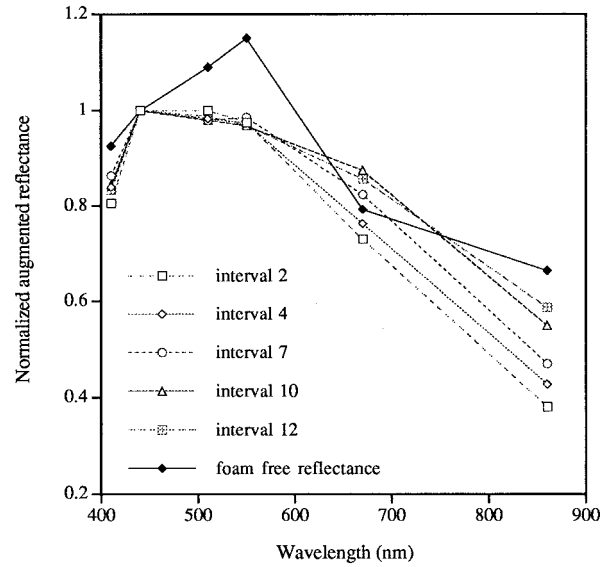

FIG. 10. Normalized augmented spectral reflectance at 440 nm for different foam types (used in Fig. 10). Note the spectral similarity for all foam types, and the increasing 670- and 860-nm values with respect to 440 nm for increasing reflectance interval from thicker fluffier foam types.

are normalized at 440 nm along with the background foam-free water reflectance. The spectral variation of different foam types can be seen by normalizing their reflectances. The foam-free water spectral reflectance shows a relatively small difference between 410 and 440 nm. The foam-free water has reflectance values of 0.0431, 0.0466, 0.0509, 0.0535, 0.0370, and 0.0310 at 410, 440, 510, 550, 670, and 860 nm, respectively. The influence of the background foam-free water reflectance can be seen particularly in the lower reflectance intervals. The 550-nm value in interval 2 is slightly higher than the 510-nm value, and the spectral shape appears to be somewhere between the foam-free water reflectance and that of a foam reflectance from a higher reflectance interval. While the slope between the 670- and 860-nm values for reflectance interval 2 is smaller than for the higher reflectance intervals, it is not quite as small as the foam-free water reflectance. The high 510- and 550-nm values in both the foam-free reflectance interval and interval 2 seem to eventually disappear in the higher reflectance intervals. Since the lower reflectance interval is comprised of the thinnest foam types, with patches of single-layered bubbles, measurements of the foam-free water will inevitably be included. With thicker and denser foam types comprising the higher reflectance intervals, the measurement of foam-free contributions decreases with increasing reflectance intervals. The probability of including the reflectance contributions from submerged bubbles also decreases with higher reflectance intervals. On the other hand, the normalized 410-nm values appear to remain the same regardless of reflectance interval.

In Fig. 10 the augmented reflectances for the same foam types used in Fig. 9 normalized at 440 nm are shown. The measure of augmented reflectance in this case simply means that the foam-free water reflectance has been subtracted from the foam reflectance in order to investigate the spectral variation with foam type only. Many features are similar to the reflectance profiles for these intervals shown in Fig. 9. As expected, with the removal of the foam-free water reflectance, the smallest reflectance interval no longer shows the similarity to the background foam-free water reflectance as it did in Fig. 9. All the spectra are essentially identical with the exception of the 670- and 860-nm values, which increase with higher reflectance interval (thicker, more-reflecting foam). Once again, the all foam spectra have a lower 410-nm value than the foam-free reflectance, and the 440-, 510-, and 550-nm values are almost equivalent, explaining the white appearance of foam. However, the values at 410 nm now appear to increase, if only very slightly, with increasing reflectance interval. Also the reflectance decrease from 440 to 860 nm in these normalized spectra can now easily be seen to decrease in a progressive manner with increasing reflectance interval, and therefore, of foam type; for reflectance interval 2 (with spectral augmented reflectance at 440 nm of 0.0597 taken from 357 samples with background foam-free water spectra subtracted) there is about a 62% decrease, for interval 4 (spectral augmented reflectance at 440 nm of 0.252 from 94 samples) it is 57%, for interval 7 (spectral augmented reflectance at 440 nm of 0.488 from 113 samples) it is about 53%, interval 10 (spectral augmented reflectance at 440 nm of 0.620 from 48 samples) is about 45%, and about 41%

at interval 12 (spectral augmented reflectance at 440 nm of 0.701 from a single sample).

From these data there appears to be a similar trend in the blue between the 440- and 410-nm values. Once again, the greatest decrease occurs for the lowest reflectance interval, although not as large as between 440 and 860 nm. For interval 2 there is about a 20% decrease compared to the foam-free reflectance decrease of about 7%. At interval 4 there is about a 16% decrease, interval 7 about a 13.5% decrease, and at intervals 10 and 12 about a 15% and 17% decrease, respectively. The reverse behavior for intervals 10 and 12 may be statistical, that is, due to insufficient data.

While the very strong absorption properties of water may explain the lower reflectance values at 860 and 670 nm, the decrease at 410 relative to 440 nm cannot be explained in this manner. The spectral absorption coefficient of this water was 0.11, 0.10, 0.065, 0.08, 0.475, and 4.3 m^{-1} at the corresponding wavelengths (C. Roesler 1995, personal communication). In the case of the red and near infrared wavelengths, it is the very strong absorption qualities of the water itself that cause the observed attenuation. In contrast, the decrease in reflectance at 410 compared to 440 nm cannot be explained simply by water absorption. Consider the small absorption increase between 410 and 440 nm compared to the much greater absorption difference between 440 and 670 nm for similar values of augmented reflectance.

5. Conclusions

A system for determining the spectral reflectance of whitecaps in the open ocean has been described and calibrated for optimum use on board a ship or other above-water surface platform. We have also tested the system to determine the possible errors that can occur in going from laboratory calibration with a lamp source (a point source) to field illumination under the solar spectrum. The calibration for different sky conditions and solar zenith angles, if not exactly represented by the real sky conditions at the time of acquisition, shows the degree of error that can be incurred without correction and indicates the degree of spectral variation that must be due to real effects in the field.

The system has been designed to acquire spectral data of real whitecaps and their frequency rather than foam generated from the ship's bow that (by necessity) became the focus of our test; however, measurements of the ship-induced foam do show that the radiometer can be successfully operated at sea for studying whitecaps. By taking many reflectance measurements of the water surface over time, a database of the spectral reflectance of different foam types and their frequency of occurrence can be assessed, providing estimates of fractional coverage and the augmented or extra spectral reflectance contribution of whitecaps and foam. Measurement of wind speed/direction and air/water temperature will provide additional information in correlating the augmented signal to these formation parameters.

Although few whitecaps were observed on the test cruise, field testing the whitecap measurement system has provided interesting information on the spectral features of foam. Examples of foam reflectance, which can generally be related to different foam types and thicknesses, have been provided and show interesting spectral features that differ from the foam-free water. The magnitude of these features are significantly greater than the error due to illumination condition, deviation of the irradiance collector from a true cosine response, filter bandwidth mismatch, or reflectance calibration of the system. Of particular interest is the decrease in reflectance between 440 and 860 nm. These results are in good agreement with the measurements reported by Frouin et al. (1996) in the surf zone in similar waters, although we find lower 670-nm values (see Figs. 9 and 10), possibly due to increased quantities of submerged bubbles generated by the ship. The greatest spectral variation is found for the thinnest foam layers (Fig. 10), where a significant contribution to the reflectance is likely to be scattering from submerged bubbles. In the case of ship foam, the bow of the ship forces and redistributes entrapped air bubbles deep below the water surface in a different manner than foam generation in the surf zone and foam generated purely by wind action. The bow is responsible for a visible increase of thick, dense clouds of submerged bubbles that could be seen through small and intermittent packets of relatively clear foam-free water. As a result, it is reasonable to assume that there is a greater proportion of such submerged bubble contributions in the lower reflectance intervals in the data acquired here. As noted before, the pronounced decrease in reflectance in the near infrared is considered to be due to the stronger absorption properties of water at the longer wavelengths, affecting light that is reflected from submerged bubbles, through a small layer of water between the bubbles and the surface (Frouin et al. 1996). In the case of surf zone white water, the majority of measurements that fall within a similar reflectance interval may be from a larger proportion of thin surface foam, which lacks the severity of the 670- and 860-nm attenuation found in ship-bow foam. It is this greater incidence of deep bubble contributions that we attribute to the lower 670- and 860-nm values than found in the surf zone.

The augmented reflectance for different foam types (Fig. 10) shows a distinct change in the spectra in going from the foam-free water reflectance to the thinnest foam measurement. It also shows a trend in which the 670- and 860-nm reflectances increase with respect to the other wavebands as the foam becomes thicker and more highly reflecting, that is, as the submerged bubble contribution decreases relative to the surface foam. The reflectance of foam without the background foam-free water reflectance subtracted (Fig. 9) shows that the water color becomes more prominent in measurement of

the thinner and lower reflecting foam types. The foam-free water reflectance influences the thinner foam spectra due to the inevitable inclusion of foam-free reflectance contributions. The use of normalized augmented reflectance, which appears to effectively remove the water color influence in these examples, may still be contaminated in the lower reflectance intervals, that is, the thinnest foam.

Acknowledgments. This research was funded by NASA/EOS -MODIS, Goddard Space Flight Center under Contract NAS5-31363. We would like to thank Al Chapin for his help in the construction of the equipment, Judd Welton for clear-sky radiance data, Collen Roesler for the water absorption coefficient data, and Dr. Alan Weidemann and crew of the R/V *McGaw* for allowing us to participate in their oceanographic excursion.

REFERENCES

Austin, R. W., and S. Moran, 1974: Reflectance of whitecaps, foam, and spray. *Ocean Color Analysis,* Scripps Institution of Oceanography, 3.1–3.10.

Bass, M., and Coeditors, 1995: *Handbook of Optics.* Vol. 1, McGraw Hill, Inc., 1447 pp.

Bortkovskii, R. S., and V. A. Novak, 1993: Statistical dependencies of sea state characteristics on water temperature and wind-wave age. *J. Mar. Syst.,* **4,** 161–169.

Chandrasekhar, S., 1950: *Radiative Transfer*. Oxford University Press, 393 pp.

Frouin, R., M. Schwindling, and P. Y. Deschamps, 1996: Spectral reflectance of sea foam in the visible and near infrared: In situ measurements and remote sensing implications. *J. Geophys. Res.,* **101,** 14 361–14 371.

Gordon, H. R., and M. M. Jacobs, 1977: Albedo of the ocean–atmosphere system: Influence of sea foam. *Appl. Opt.,* **16,** 2257–2260.

——, and M. Wang, 1994a: Retrieval of water-leaving radiance and aerosol optical thickness over the oceans with SeaWiFS: A preliminary algorithm. *Appl. Opt.,* **33,** 443–452.

——, and ——, 1994b: Influence of oceanic whitecaps on atmospheric correction of SeaWiFS. *Appl. Opt.,* **33,** 7754–7763.

Holben, B. N., and Coauthors, 1997: Automatic sun and sky scanning radiometer system for network aerosol monitoring. *Remote Sens. Environ.,* in press.

Koepke, P., 1984: Effective reflectance of oceanic whitecaps. *Appl. Opt.,* **23,** 1816–1824.

Maul, G. A., and H. R. Gordon, 1975: On the use of earth resources technology satellite (*LANDSAT-1*) in optical oceanography. *Remote Sens. Environ.,* **4,** 95.

Monahan, E. C., 1971: Oceanic whitecaps. *J. Phys. Oceanogr.,* **1,** 139–144.

Moore, K. D., K. J. Voss, and H. R. Gordon, 1997: Spectral reflectance of whitecaps: Fractional coverage and the augmented spectral reflectance contribution to water leaving radiance. *J. Geophys. Res.,* in press.

Payne, R. E., 1972: Albedo of the sea surface. *J. Atmos. Phys.,* **29,** 959–970.

Ross, D. B., and V. J. Cardonne, 1974: Observations of oceanic whitecaps and their relation to remote measurements of surface wind speed. *J. Geophys. Res.,* **79,** 444–452.

Stabeno, P. J., and E. C. Monahan, 1986: The influence of whitecaps on the albedo of the sea surface. *Oceanic Whitecaps,* E. C. Monahan and G. M. Niocaill, Eds., Reidel, 261–266.

Toba, Y., and M. Chaen, 1973: Quantitative expression of the breaking of wind waves on the sea surface. *Rec. Oceanogr. Works,* **12,** 1–11.

Whitlock, C. H., D. S. Bartlett, and E. A. Gurganus, 1982: Sea foam reflectance and influence on optimum wavelength for remote sensing of ocean aerosols. *Geophys. Res. Lett.,* **9,** 719–722.